High-mobility transport in isotopically enriched ^{12}C and ^{13}C exfoliated graphene

Shuichi Iwakiri,[1,*] Jakob Miller,[1] Florian Lang,[1] Jakob Prettenthaler,[1] Takashi Taniguchi,[2] Kenji Watanabe,[3]
Sung Sik Lee,[4] Pascal Becker,[5] Detlef Günther,[5] Thomas Ihn,[1,6] and Klaus Ensslin[1,6]
[1]*Solid State Physics Laboratory, ETH Zurich, CH-8093 Zurich, Switzerland*
[2]*Research Center for Materials Nanoarchitectonics, National Institute for Materials Science, 1-1 Namiki, Tsukuba 305-0044, Japan*
[3]*Research Center for Electronic and Optical Materials, National Institute for Materials Science, 1-1 Namiki, Tsukuba 305-0044, Japan*
[4]*ScopeM, ETH Zurich, CH-8093 Zurich, Switzerland*
[5]*Department of Chemistry and Applied Biosciences, ETH Zurich, CH-8093 Zurich, Switzerland*
[6]*Quantum Center, ETH Zurich, CH-8093 Zurich, Switzerland*

(Received 16 August 2023; accepted 6 November 2023; published 7 December 2023)

Graphene quantum dots are promising candidates for qubits due to weak spin-orbit and hyperfine interactions. The hyperfine interaction, controllable via isotopic purification, could be the key to further improving the coherence. Here, we use isotopically enriched graphite crystals of both ^{12}C and ^{13}C grown by a high-pressure-high-temperature method to exfoliate graphene layers. We fabricated Hall bar devices and performed quantum transport measurements, revealing mobilities exceeding 10^5 cm^2/V s and a long mean free path of microns, which are as high as natural graphene. Shubnikov–de Haas oscillations, quantum Hall effect up to the filling factor of one, and Brown-Zak oscillations due to the alignment of hBN and graphene are observed thanks to the high mobility. These results constitute a material platform for physics and engineering of isotopically enriched graphene qubits.

DOI: 10.1103/PhysRevResearch.5.043212

I. INTRODUCTION

Graphene quantum dots are among the most promising candidates as platforms for spin qubits [1–3] thanks to the weak spin-orbit coupling and hyperfine interactions. Understanding the hyperfine interaction is a strategy to improve the qubit coherence in several systems such as GaAs [4–7] and Si-based systems [8–10]. The hyperfine interaction has also been investigated in ^{13}C-enriched carbon nanotube quantum dots [11] and it was theoretically proposed that graphene quantum dots could benefit from isotope purification [1,12–14], modulating the ratio of ^{12}C (nuclear spin 0) and ^{13}C (nuclear spin 1/2) (see Appendix A). Comparing the results of ^{12}C and ^{13}C enrichment would enable the direct investigation of the effect of hyperfine interaction. Isotopically enriched graphene has been realized by the chemical vapor deposition (CVD) method [15,16]. High-quality single layer graphene has been fabricated by the same method [17], while it remains difficult to produce bilayer graphene by CVD growth.

In this work, we investigate high-quality exfoliated graphene devices out of ^{12}C-enriched (99.7%) and ^{13}C-enriched (91.4%) graphites. We synthesize enriched graphite by the high-pressure-high-temperature method [18,19]. We then establish a recipe to exfoliate the layered crystals to obtain monolayer and bilayer graphene. The isotope effect is characterized by mass spectroscopy and Raman spectroscopy, showing a clear difference between ^{12}C and ^{13}C graphene. After confirming the enrichment, we fabricate a Hall bar device from each kind of graphite and perform quantum transport measurements. For both graphene samples, high mobility ($\mu \geqslant 1 \times 10^5$ cm^2/V s) and long mean free path ($l_{\mathrm{mfp}} \geqslant 1$ μm) are demonstrated. These values demonstrate that the electronic quality of graphene remains as high as natural graphene after isotopic enrichment. We also observe the Shubnikov–de Haas oscillations, quantum Hall effect, and Brown-Zak oscillations, which confirm the quality of the sample. While all of these observations constitute well-known properties of graphene their appearance in samples derived by isotopically purified carbon crystals is by no means obvious. This result forms the basis for building isotopically enriched graphene qubits and investigating the role of hyperfine interactions.

II. CHARACTERIZATION RESULTS

A. Enriched graphite and exfoliation

Figure 1(a) shows the optical picture of the crystal of ^{12}C-enriched and ^{13}C-enriched graphite. Hereafter, we call them ^{12}C graphite/graphene and ^{13}C graphite/graphene for convenience. For ^{12}C and ^{13}C isotope-enriched graphite, the conditions for diamond single-crystal growth and synthesis were carried out in the pressure and temperature range where graphite is stable [20]. Namely, at 4 GPa and 1600 °C, Co-Ti alloy was used as a solvent and carbon isotope-enriched carbon source as a starting material; ^{12}C-enriched carbon was

---

[*] siwakiri@phys.ethz.ch

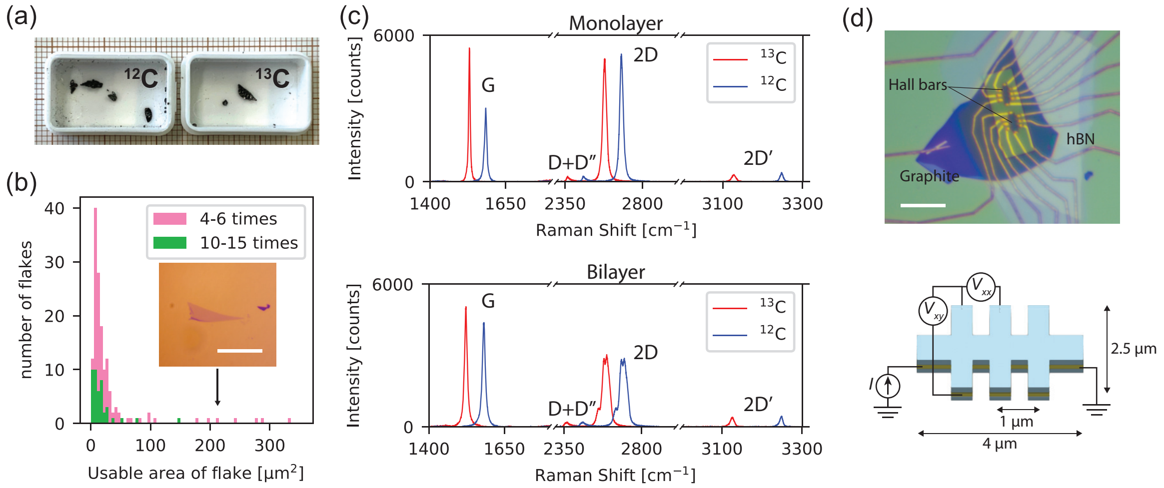

FIG. 1. (a) Optical picture of ^{12}C and ^{13}C graphite crystals. The minimum grid size in the background is 1 mm. (b) Histogram of ^{12}C graphene flake size. Inset shows a picture of the example bilayer flake. The scale bar is 50 μm. (c) Raman spectrum of ^{12}C and ^{13}C graphene. Top: monolayer graphene. Bottom: bilayer graphene. (d) Top panel: optical picture of the fabricated Hall bar. The scale bar is 10 μm. Bottom panel: schematic of the fabricated Hall bar.

thermal CVD diamond from Tomei Diamond, using methane gas with 99.998% ^{12}C as a starting material; ^{13}C enriched was commercial amorphous graphite powder with purity of 99% (Cambridge Isotope Laboratories, Inc). After HP-HT synthesis, recovered graphite single crystals with metal solvent were treated with hot aqua regia for purification.

Note that the crystal size (∼5 mm) is relatively small compared to the natural graphite crystals, which can be up to the order of cm. The relative isotope ratio found in the crystals is determined using inductively coupled plasma time-of-flight mass spectrometry (ICP-TOFMS). The ICP-TOFMS (icp-TOF2R, TOFWERK AG, Thun, Switzerland) is operated in low-mass mode and was coupled to an ArF excimer laser (193 nm, GeoLas C, Lambda Physik, Göttingen), equipped with a low dispersion ablation cell for minimally invasive sampling of the small crystals. The ratios of isotopes are determined for natural graphite, ^{12}C graphite, and ^{13}C graphite. The results of the natural graphite are used to calibrate the ratio for the other samples, assuming the natural abundance of $^{12}\mathrm{C} : {}^{13}\mathrm{C} = 98.9 : 1.1$. The result of the mass spectroscopy yields $^{12}\mathrm{C} : {}^{13}\mathrm{C} = 99.7 : 0.3$ for the ^{12}C sample and $8.6 : 91.4$ for the ^{13}C sample, confirming the effect of enrichment. The relative concentrations of the isotopes determined by mass spectroscopy have a relatively large error because of the small amount of the sample available.

In spite of the relatively small size of the graphite crystals, exfoliation is possible for both ^{12}C and ^{13}C. We perform exfoliation by using the standard scotch tape method, where we deposit graphite onto the scotch tape and fold and peel apart the tape a certain number of times before the flakes are transferred onto a Si/SiO2 substrate (with an oxide thickness of 285 nm). We compare exfoliation for folding and peeling apart the tape 4–6 times with 10–15 times. We analyze the chips under a microscope and record the size of the flakes. The statistics of the flake size (mono-, bi-, and trilayer ^{12}C graphene) is shown in Fig. 1(b), together with an image of an example of a large bilayer flake. It turns out that after 4–6 times of exfoliation, it is possible to obtain 50 μm scale graphene flakes of mono-, bi-, and trilayers. The same result is obtained for the ^{13}C graphene. These results demonstrate that the enriched ^{12}C and ^{13}C exfoliation is possible and that the flakes are available for fabricating devices.

B. Raman spectroscopy

The exfoliated graphene is further characterized by Raman spectroscopy (Horiba LabRAM HR Evolution UV-VIS-NIR). The laser energy and wavelength are 1 mW and 532 nm, respectively. We choose a flake larger than 10 μm and perform a Raman spectrum measurement by changing the laser position. The data shown in Fig. 1(c) is from the part of the graphene that is a few μm inside from the edge of the flake. The measurements are done on mono- and bilayer flakes. As shown in Fig. 1(c), both ^{12}C and ^{13}C graphene show prominent G (∼1520–1580 cm^{-1}), D+D″ (∼2360–2490 cm^{-1}), 2D (∼2540–2710 cm^{-1}), and 2D′ (∼3120–3250 cm^{-1}) peaks. The numbers in the parentheses are typical ranges of the observed peak wave numbers. We see a clear peak wave number shift between ^{12}C and ^{13}C. These differences are one of the most prominent signatures of the isotope effect because the nuclear mass difference results in a phonon frequency and Raman shift difference. We do not observe a shift between ^{12}C and natural graphene within the experimental resolution. After subtracting a linear background from the data, we fit all the peaks with Lorentzian functions. The fit parameters are in Table I in Appendix B.

The obtained parameters are consistent with the ones reported in exfoliated natural graphene and isotopically enriched CVD graphene [21–27]. The measured wave number of the G peak, ω_G, for ^{12}C or natural graphene reported in Refs. [21–25] are between $-2\,\mathrm{cm}^{-1}$ and $+10\,\mathrm{cm}^{-1}$ of our measured values for ^{12}C graphene (for mono- and bilayer). The ω_G for ^{13}C graphene reported in [23,25] is in the range of $-5\,\mathrm{cm}^{-1}$ to $+8\,\mathrm{cm}^{-1}$ of the values we measure for mono- or bilayer. Comparing the wave number of the 2D peak, ω_{2D}, to literature values, it turns out that the values reported are

TABLE I. Fit parameters for the Raman peaks. We fit the data with the sum of one to three Lorentzian functions (in the case we use multiple Lorentzian to fit, all fit parameters are shown in order and separated by comma).

Layers Material	1 ^{12}C	1 ^{13}C	2 ^{12}C	2 ^{13}C
ω_G (cm^{-1})	1584	1530	1581	1522
Γ_G (cm^{-1})	8.143	5.316	11.14	9.983
ω_{2D} (cm^{-1})	2678	2580	2646, 2681, 2704	2546, 2580, 2602
Γ_{2D} (cm^{-1})	21.431	22.296	14.98, 21.76, 31.32	13.49, 21.47, 29.96
$\omega_{2D'}$ (cm^{-1})	3247	3128	3248	3125
$\Gamma_{2D'}$ (cm^{-1})	8.455	11.274	8.709	10.61
$\omega_{D+D''}$ (cm^{-1})	2479, 2457	2366, 2388	2458, 2489	2365, 2394
$\Gamma_{D+D''}$ (cm^{-1})	41.27, 15.29	14.41, 36.46	26.04, 48.69	21.82, 41.55

generally slightly higher (up to 1.5%) than the values we measure. For the monolayer ^{12}C graphene ω_{2D}, we find that our measurement aligns very well (within 1 cm^{-1}) with the natural graphene measurement in [21]. However, the measurements in Refs. [23–25] find values 15–35 cm^{-1} higher than what we measure for ^{12}C monolayer graphene as well as for ^{13}C monolayer graphene. Looking at the bilayer measurements for ω_{2D} peaks [21], we find two peaks that are 2 cm^{-1} and 3 cm^{-1} apart. For $\omega_{2D'}$ Ref. [28] reports 3250 cm^{-1} for ^{12}C graphene and 3130 cm^{-1} for ^{13}C graphene. These values are consistent with what we measure.

We also estimate the isotopic concentration of ^{13}C graphene from the Raman shift using the relation $\omega = \omega_{12\mathrm{C}}\sqrt{\frac{m}{m+x\Delta m}}$ [29]. Here, $\omega_{12\mathrm{C}}$ is the Raman shift of pure ^{12}C graphene, m is the atomic mass of ^{12}C, x is the concentration of ^{13}C, and Δm is the atomic mass difference of ^{12}C and ^{13}C. For ^{13}C graphene, we obtain a ^{13}C enrichment $x = 92.9\%$ using the 2D and 2D′ peaks and $x = 86.2\%$ using the G peak. Since the G peak is sensitive to the distortion and carrier density [30], it can be affected by unintentional doping due to the charged impurity in the silicon substrate, making the peak shift. The estimation from 2D and 2D′ peaks is closer to the value obtained by the mass spectroscopy with a slight overestimation (±1.5%). At around 93% of ^{13}C, the deviation of Raman shifts by one cm^{-1} modulates the concentration estimation by ∼1.7%. Therefore, considering the resolution of the measurement, the estimation from the 2D and 2D′ peaks is consistent with the one from the mass spectroscopy.

C. Device fabrication

To characterize the transport quality of the isotopically enriched graphene, we fabricate Hall bars of ^{12}C and ^{13}C bilayer graphene as shown in Fig. 1(d). A stack of hexagonal boron-nitride (top hBN)/bilayer graphene/hBN (bottom hBN)/graphite (back gate) is made by the polydimethylsiloxane/polycarbonates dry transfer method. Thicknesses of top and bottom hBN are 12 nm and 18 nm for the ^{12}C sample and 20 nm and 30 nm for the ^{13}C one. Electric contacts to the edge of the bilayer graphene are fabricated by etching the top hBN and depositing Cr/Au. After etching, a Hall bar is shaped by reactive ion etching (CHF$_3$ and O$_2$). We measure the Hall bars in a dilution refrigerator with a base temperature of 55 mK. The bottom panel of Fig. 1(d) shows the schematic of the device. The two contacts at each sample end are used as source and drain electrodes, where we inject current from the source to the grounded drain. The longitudinal and transverse voltages (V_x and V_y) are measured between the two contacts along and across the sides. The spacing between source and drain and between the voltage contacts is 4 µm and 1 µm, respectively. We use a lock-in amplifier (Stanford Research Systems SR830) connected to the source in series with a 100 MΩ resistance and apply an ac voltage of 1 V, generating an ac current of 10 nA. We synchronize the lock-in amplifier driving the current I with the other two lock-in amplifiers. These lock-in amplifiers are then used to measure the resistances ($R_{xx} = \frac{dV_x}{dI}$ and $R_{xy} = \frac{dV_y}{dI}$ at zero bias current). We apply a dc voltage (Yokogawa 7651 Programmable dc Source) to the back gate (not shown in the schematic).

III. TRANSPORT MEASUREMENT

Figures 2(a) and 2(d) show the magnetic field B and the carrier density n dependence of the longitudinal resistance R_{xx} of ^{12}C and ^{13}C devices. The carrier density on the horizontal axis is estimated by measuring the classical Hall effect up to 100 mT and using the relation $R_{xy} = \frac{B}{n|e|}$. We also obtain consistent values from a parallel plate capacitor model ($n = C_{\mathrm{bg}}V_{\mathrm{bg}}$, where C_{bg} is the capacitance between the graphene and the back gate and V_{bg} is the back gate voltage) and Shubnikov–de Haas measurements [$R_{xx} \propto \cos(\frac{2\pi nh}{4eB})$].

For both samples, clear fanlike structures departing from the charge neutrality point $n = 0$ and expanding with magnetic field are seen, which is attributed to the Shubnikov–de Haas (SdH) oscillations. The oscillations appear already at around 1 T, testifying to our samples' high mobility. White dotted tilted lines show the fitting to the filling factor of 1, 2, and 3 at around $n = 0$ (for ^{12}C and ^{13}C) and filling factor for 2, 6, and 10 at around $n = \pm 2.3 \times 10^{12}$ cm^{-2} (for ^{12}C only).

Additionally, in the ^{12}C sample, we see multiple Landau fans appearing at densities of around 4.09, 3.29, 2.30, 1.78, −2.06, and -2.31×10^{12} cm^{-2}. This is attributed to the additional Dirac points due to the unintended alignment between the graphene and one of the hBNs, forming a moiré superlattice [31]. This results in an energy spectrum for the charge carriers known as the Hofstadter butterfly and causes satellite Dirac peaks. Furthermore, at the intersections of the Landau

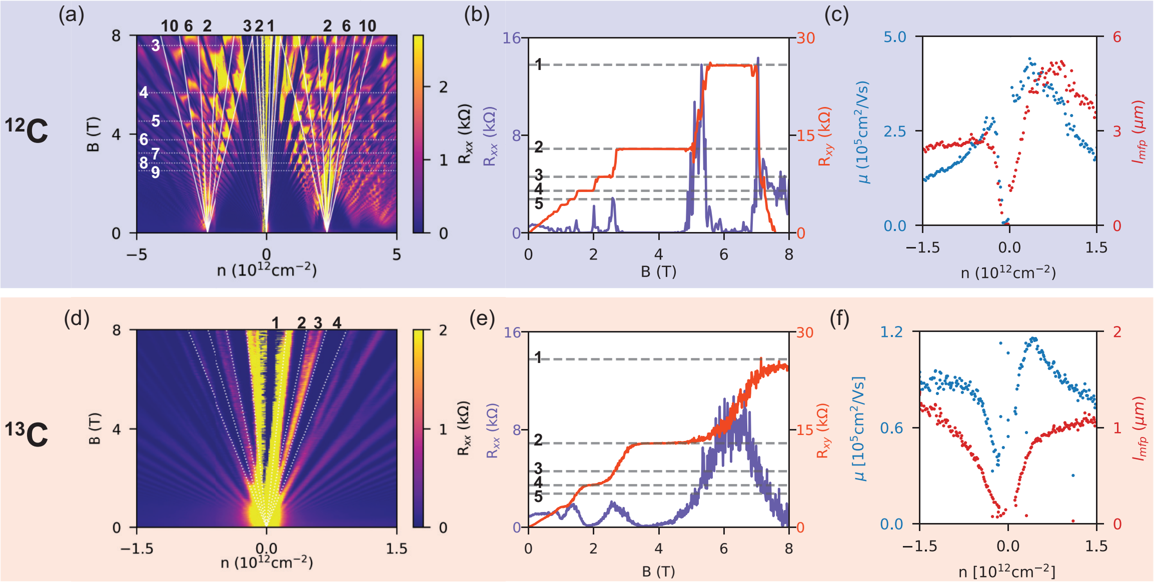

FIG. 2. Quantum transport measurement of ^{12}C (a),(b),(c) and ^{13}C (d),(e),(f) bilayer graphene. (a),(d) R_{xx} as a function of magnetic field B and carrier density n. White dotted tilted lines fit the Shubnikov–de Haas oscillations with filling factors shown in the figure. White dotted horizontal lines show the position at which the Brown-Zak oscillations appear. (b),(e) Example traces of the quantum Hall effect at $n = 1.13 \times 10^{11}$ (^{12}C) and $n = 1.9 \times 10^{11}$ (^{13}C). (c),(f) Carrier density n dependence of the mobility μ and the mean free path $l_{\rm mfp}$ estimated from the low magnetic field data.

fans, it predicts horizontal lines of peaks in R_{xx} called Brown-Zak oscillations [32–34]. The horizontal lines in Fig. 2(a) indicate the position of $\phi/\phi_0 = 1/p$ with p an integer and $\phi_0 = h/e$ the flux quanta. As we discuss in Appendix C, the moiré unit cell size estimated from the Brown-Zak oscillations agrees with the one formed by graphene/hBN alignment. This observation is another piece of evidence for having a high-quality sample.

At a high magnetic field, we observe the quantum Hall effect, as shown in Figs. 2(b) and 2(e). For both samples, the integer quantum Hall effect is observed up to filling factor $\nu = 1$ with quantized plateaus of R_{xy} and dips of R_{xx}. The significant drop of R_{xy} in ^{12}C beyond filling factor 1 ($B \geqslant 7$ T) is due to the Brown-Zak oscillations. We observe a similar drop whenever B crosses the horizontal lines indicated in Fig. 2(a).

We also estimate the mobility μ and mean free path $l_{\rm mfp}$ by applying the classical Drude model to $\rho_{xx} = \frac{W}{L} R_{xx}$ (W and L are the width and the length of the sample) and $\rho_{xy} = R_{xy}$ at a low magnetic field ($\leqslant$100 mT). From the slope of the linear fit of R_{xy} up to 100 mT together with R_{xx} at 0 T, we determine μ and $l_{\rm mfp}$ using the equations $\mu = \frac{1}{\rho_{xx}(B=0)} \frac{d\rho_{xy}}{dB}$ and $l_{\rm mfp} = \frac{\hbar\sqrt{\pi n}}{|e|}\mu$. As seen in Figs. 2(c) and 2(f), the mobility mostly ranges from 1×10^4 to 3×10^5 cm^2/V s. The mobility becomes zero around charge neutrality and forms a peak with increasing n. This behavior can be attributed to the difference in dominant scattering mechanisms (long-range Coulomb scattering at low density and short-range impurity scattering at high density) [35].

The mean free path $l_{\rm mfp}$ reaches up to 1–5 μm for both ^{12}C and ^{13}C. This value is comparable to the one reported in natural graphene. Note that the spacing between the contacts is of the same order of magnitude as the estimated mean free path, meaning that the transport in the sample is in the ballistic regime. In this regime, the Drude model has limited validity and the mobility and mean free path are lower bound estimates.

Up to now, our results of transport measurement do not show significant differences between ^{12}C and ^{13}C. We further perform a quantum Hall effect breakdown measurement, applying a dc current up to 10 μA so that the quantum Hall effect (plateau in ρ_{xy} and zero in ρ_{xx}) is no longer observed. In GaAs 2DEG systems, a large hysteresis in the current sweep direction before and after the breakdown is observed typically for odd filling factors due to dynamic nuclear polarization (spin transfer from electrons to nuclei) [36,37]. We do not observe any clear hysteresis within our measurement precision (data is not shown here). To observe the effect of hyperfine interaction, more sophisticated measurements such as resistivity-detected NMR [38–40] or actually building a quantum dot and performing a T_1 and T_2 coherence time measurement would be useful.

IV. CONCLUSION

In conclusion, we have presented high-mobility transport of exfoliated ^{12}C and ^{13}C graphene synthesized by the high-pressure-high-temperature technique. We confirmed distinct differences between ^{12}C and ^{13}C graphene by the mass and Raman spectroscopy. We also fabricated Hall bar devices and performed quantum transport measurements, revealing high mobility and a long mean free path of these materials comparable to the natural graphene. Shubnikov–de Haas, quantum Hall, and Brown-Zak effects up to the filling factor of one were observed thanks to the high mobility. These results pave the way for developing isotopically enriched graphene qubits and investigating the role of hyperfine interactions in graphene quantum dots.

ACKNOWLEDGMENTS

We are grateful for fruitful discussions and technical support from L. Ginzburg, C. Tong, M. Niese, P. Maerki, T. Baehler, and the ETH FIRST cleanroom facility staff. We acknowledge financial support by the European Graphene Flagship Core3 Project, H2020 European Research Council (ERC) Synergy Grant under Grant Agreement No. 951541, the European Union's Horizon 2020 research and innovation programme under Grant Agreement No. 862660/QUANTUM E LEAPS, the European Innovation Council under Grant Agreement No. 101046231/FantastiCOF, and NCCR QSIT (Swiss National Science Foundation, Grant No. 51NF40-185902). K.W. and T.T. acknowledge support from the JSPS KAKENHI (Grants No. 21H05233 and No. 23H02052) and World Premier International Research Center Initiative (WPI), MEXT, Japan.

APPENDIX A: COHERENCE TIME ESTIMATION

Following the steps of [1], we studied the effect of isotopic composition on the lifetime τ of coherent spin states (T_2) in graphene quantum dot qubits. While the different atomic masses of ^{12}C and ^{13}C may affect the spin-orbit coupling, it is believed that the hyperfine interaction limits the coherence time in graphene [1]. The limit on the coherence time set by the hyperfine interaction (hyperfine coherence time) τ_{hf} depends on the composition of the spinless ^{12}C and the spin-1/2 ^{13}C. It can be estimated from the hyperfine coupling strength $A_{\text{hf}} = 0.38\,\mu\text{eV}$, the ^{13}C concentration c_{13C}, and the number of atoms in a dot N using $\tau_{\text{hf}} = \frac{h}{A_{\text{hf}}}\sqrt{N/c_{13C}}$.

Compared to natural graphene ($c_{13C} = 1.1\%; N = 10^4$: $\tau_{\text{hf}} \approx 10\ \mu\text{s}$) the purification level of our ^{12}C sample ($c_{13C} = 0.3\%$) would already increase the hyperfine coherence time by a factor of two. Further decreasing the ^{13}C concentration (99.99% purified ^{12}C), would increase the coherence time by another factor of five, to around $\tau_{\text{hf}} \approx 100\,\mu\text{s}$. This shows the strong sensitivity of the hyperfine coherence time on isotopic composition at low ^{12}C concentrations. For a dot size of $N = 10^4$ atoms, this purification level of 99.99% would already mean that on average just one ^{13}C atom would be present per dot. By selecting the dots without any ^{13}C and thus no nuclear spins, one can completely lift the limitation of the coherence time by the hyperfine interaction.

APPENDIX B: RAMAN PEAKS FITTING PARAMETERS

We fitted the Raman spectrum with Lorentzian function $\frac{A\Gamma^2}{(\omega-\omega_0)^2+\Gamma^2}$, where A is the peak amplitude, k is the wave number, k_0 is the peak wave number, and Γ is the linewidth (half width at half maximum). The results are shown below. We used a single Lorentzian function for G and $2D'$ peaks, the sum of two Lorentzian functions for the $D + D''$ peak, and the sum of three Lorentzian functions for the $2D$ peak.

APPENDIX C: ESTIMATION OF MOIRÉ UNIT CELL SIZE FROM THE BROWN-ZAK OSCILLATION

We have estimated the moiré cell size with two approaches. First, since the satellite Dirac peaks appear once all the available states in the moiré cell are filled, we can determine the area A of the moiré cell from the average of the excess carrier density of the electron- and hole-side peaks $n_{ep} = 1.78 \times 10^{12}\ \text{cm}^{-2}$ and $n_{hp} = -2.31 \times 10^{12}\ \text{cm}^{-2}$. Considering the fourfold degeneracy in graphene, this condition corresponds to $A = \frac{4}{\frac{1}{2}(|n_{ep}|+|n_{hp}|)}$. The second approach uses the periodicity of the Brown-Zak oscillations, which appear if a rational number $1/p$ of flux quanta ϕ_0 (p is an integer) passes through one moiré cell. The moiré cell area can then be determined from the positions of two adjacent Brown-Zak peaks in magnetic field (B_1 and B_2) using $A = \phi_0|\frac{1}{B_1} - \frac{1}{B_2}|$. The lattice constant can be obtained from the area by simple geometric considerations such as $L = \sqrt{2A/\sqrt{3}}$. Both methods give a consistent estimate of the moiré unit cell size of 10 nm, which is reasonable for the graphene/hBN-aligned system.

[1] B. Trauzettel, D. V. Bulaev, D. Loss, and G. Burkard, Spin qubits in graphene quantum dots, Nat. Phys. **3**, 192 (2007).

[2] M. Eich, R. Pisoni, A. Pally, H. Overweg, A. Kurzmann, Y. Lee, P. Rickhaus, K. Watanabe, T. Taniguchi, K. Ensslin, and T. Ihn, Coupled quantum dots in bilayer graphene, Nano Lett. **18**, 5042 (2018).

[3] L. Banszerus, K. Hecker, S. Möller, E. Icking, K. Watanabe, T. Taniguchi, C. Volk, and C. Stampfer, Spin relaxation in a single-electron graphene quantum dot, Nat. Commun. **13**, 3637 (2022).

[4] J. R. Petta, A. C. Johnson, J. M. Taylor, E. A. Laird, A. Yacoby, M. D. Lukin, C. M. Marcus, M. P. Hanson, and A. C. Gossard, Coherent manipulation of coupled electron spins in semiconductor quantum dots, Science **309**, 2180 (2005).

[5] L. C. Camenzind, L. Yu, P. Stano, J. D. Zimmerman, A. C. Gossard, D. Loss, and D. M. Zumbühl, Hyperfine-phonon spin relaxation in a single-electron GaAs quantum dot, Nat. Commun. **9**, 3454 (2018).

[6] T. Fujita, P. Stano, G. Allison, K. Morimoto, Y. Sato, M. Larsson, J.-H. Park, A. Ludwig, A.D. Wieck, A. Oiwa, and S. Tarucha, Signatures of hyperfine, spin-orbit, and decoherence effects in a Pauli spin blockade, Phys. Rev. Lett. **117**, 206802 (2016).

[7] S. I. Erlingsson and Y. V. Nazarov, Hyperfine-mediated transitions between a Zeeman split doublet in GaAs quantum dots: The role of the internal field, Phys. Rev. B **66**, 155327 (2002).

[8] K. Eng, T. D. Ladd, A. Smith, M. G. Borselli, A. A. Kiselev, B. H. Fong, K. S. Holabird, T. M. Hazard, B. Huang, P. W. Deelman, I. Milosavljevic, A. E. Schmitz, R. S. Ross, M. F.

Gyure, and A. T. Hunter, Isotopically enhanced triple-quantum-dot qubit, Sci. Adv. **1**, e1500214 (2015).

[9] A. M. Tyryshkin, S. Tojo, J. J. L. Morton, H. Riemann, N. V. Abrosimov, P. Becker, H.-J. Pohl, T. Schenkel, M. L. W. Thewalt, K. M. Itoh, and S. A. Lyon, Electron spin coherence exceeding seconds in high-purity silicon, Nat. Mater. **11**, 143 (2012).

[10] K. M. Itoh and H. Watanabe, Isotope engineering of silicon and diamond for quantum computing and sensing applications, MRS Commun. **4**, 143 (2014).

[11] H. O. H. Churchill, A. J. Bestwick, J. W. Harlow, F. Kuemmeth, D. Marcos, C. H. Stwertka, S. K. Watson, and C. M. Marcus, Electron–nuclear interaction in ^{13}C nanotube double quantum dots, Nat. Phys. **5**, 321 (2009).

[12] J. Fischer, B. Trauzettel, and D. Loss, Hyperfine interaction and electron-spin decoherence in graphene and carbon nanotube quantum dots, Phys. Rev. B **80**, 155401 (2009).

[13] S. Sengupta, T. Frederiksen, and G. Giedke, Hyperfine interactions in open-shell planar sp^2-carbon nanostructures, Phys. Rev. B **107**, 224433 (2023).

[14] O. V. Yazyev, Hyperfine interactions in graphene and related carbon nanostructures, Nano Lett. **8**, 1011 (2008).

[15] V. Strenzke, J. M. Meyer, I. Grandt-Ionita, M. Prada, H.-S. Kim, M. Heilmann, J. M. J. Lopes, L. Tiemann, and R. H. Blick, Nuclear-induced dephasing and signatures of hyperfine effects in isotopically purified ^{13}C graphene, Phys. Rev. B **105**, 144303 (2022).

[16] M. Wojtaszek, I. J. Vera-Marun, E. Whiteway, M. Hilke, and B. J. van Wees, Absence of hyperfine effects in ^{13}C-graphene spin-valve devices, Phys. Rev. B **89**, 035417 (2014).

[17] L. Banszerus, M. Schmitz, S. Engels, M. Goldsche, K. Watanabe, T. Taniguchi, B. Beschoten, and C. Stampfer, Ballistic transport exceeding 28 micrometer in CVD grown graphene, Nano Lett. **16**, 1387 (2016).

[18] T. Taniguchi and S. Yamaoka, Spontaneous nucleation of cubic boron nitride single crystal by temperature gradient method under high pressure, J. Cryst. Growth **222**, 549 (2001).

[19] T. Taniguchi and K. Watanabe, Synthesis of high-purity boron nitride single crystals under high pressure by using Ba–BN solvent, J. Cryst. Growth **303**, 525 (2007).

[20] M. Miyakawa, C. Shinei, and T. Taniguchi, Nitrogen concentration control in diamonds grown in Co–(Fe)–Ti/Al solvents under high-pressure and high-temperature, Jpn. J. Appl. Phys. **61**, 045507 (2022).

[21] D. Graf, F. Molitor, K. Ensslin, C. Stampfer, A. Jungen, C. Hierold, and L. Wirtz, Spatially resolved Raman spectroscopy of single- and few-layer graphene, Nano Lett. **7**, 238 (2007).

[22] C. Neumann, S. Reichardt, P. Venezuela, M. Drögeler, L. Banszerus, M. Schmitz, K. Watanabe, T. Taniguchi, F. Mauri, B. Beschoten, S. V. Rotkin, and C. Stampfer, Raman spectroscopy as probe of nanometre-scale strain variations in graphene, Nat. Commun. **6**, 8429 (2015).

[23] J. Ek-Weis, S. Costa, O. Frank, and M. Kalbac, Heating isotopically labeled Bernal stacked graphene: A Raman spectroscopy study, J. Phys. Chem. Lett. **5**, 549 (2014).

[24] J. Sonntag, K. Watanabe, T. Taniguchi, B. Beschoten, and C. Stampfer, Charge carrier density dependent Raman spectra of graphene encapsulated in hexagonal boron nitride, Phys. Rev. B **107**, 075420 (2023).

[25] E. del Corro, M. Kalbac, C. Fantini, O. Frank, and M. A. Pimenta, Isotopic ^{13}C/^{12}C effect on the resonant Raman spectrum of twisted bilayer graphene, Phys. Rev. B **88**, 155436 (2013).

[26] E. Whiteway, S. Bernard, V. Yu, D. G. Austing, and M. Hilke, The Graphene Phonon Dispersion with C12 and C13 Isotopes, *AIP Conf. Proc. No. 1566* (AIP, Melville, NY, 2013), pp. 135–136.

[27] E. Whiteway, M. Lee, and M. Hilke, Real-space Raman spectroscopy of graphene isotope superlattices, Phys. Rev. B **102**, 235429 (2020).

[28] S. D. Costa, J. E. Weis, O. Frank, M. Fridrichová, and M. Kalbac, Addressing Raman features of individual layers in isotopically labeled Bernal stacked bilayer graphene, 2D Mater. **3**, 025022 (2016).

[29] B. R. Carvalho, Y. Hao, A. Righi, J. F. Rodriguez-Nieva, L. Colombo, R. S. Ruoff, M. A. Pimenta, and C. Fantini, Probing carbon isotope effects on the Raman spectra of graphene with different ^{13}C concentrations, Phys. Rev. B **92**, 125406 (2015).

[30] A. Das, S. Pisana, B. Chakraborty, S. Piscanec, S. K. Saha, U. V. Waghmare, K. S. Novoselov, H. R. Krishnamurthy, A. K. Geim, A. C. Ferrari, and A. K. Sood, Monitoring dopants by Raman scattering in an electrochemically top-gated graphene transistor, Nat. Nanotechnol. **3**, 210 (2008).

[31] M. Yankowitz, J. Xue, D. Cormode, J. D. Sanchez-Yamagishi, K. Watanabe, T. Taniguchi, P. Jarillo-Herrero, P. Jacquod, and B. J. LeRoy, Emergence of superlattice Dirac points in graphene on hexagonal boron nitride, Nat. Phys. **8**, 382 (2012).

[32] B. Hunt, J. D. Sanchez-Yamagishi, A. F. Young, M. Yankowitz, B. J. LeRoy, K. Watanabe, T. Taniguchi, P. Moon, M. Koshino, P. Jarillo-Herrero, and R. C. Ashoori, Massive Dirac fermions and Hofstadter butterfly in a van der Waals heterostructure, Science **340**, 1427 (2013).

[33] R. Huber, M.-N. Steffen, M. Drienovsky, A. Sandner, K. Watanabe, T. Taniguchi, D. Pfannkuche, D. Weiss, and J. Eroms, Band conductivity oscillations in a gate-tunable graphene superlattice, Nat. Commun. **13**, 2856 (2022).

[34] R. K. Kumar, X. Chen, G. H. Auton, A. Mishchenko, D. A. Bandurin, S. V. Morozov, Y. Cao, E. Khestanova, M. B. Shalom, A. V. Kretinin, K. S. Novoselov, L. Eaves, I. V. Grigorieva, L. A. Ponomarenko, V. I. Fal'ko, and A. K. Geim, High-temperature quantum oscillations caused by recurring Bloch states in graphene superlattices, Science **357**, 181 (2017).

[35] J. H. Gosling, O. Makarovsky, F. Wang, N. D. Cottam, M. T. Greenaway, A. Patanè, R. D. Wildman, C. J. Tuck, L. Turyanska, and T. M. Fromhold, Universal mobility characteristics of graphene originating from charge scattering by ionised impurities, Commun. Phys. **4**, 30 (2021).

[36] A. M. Song and P. Omling, Strong, ultranarrow peaks of longitudinal and Hall resistances in the regime of breakdown of the quantum Hall effect, Phys. Rev. Lett. **84**, 3145 (2000).

[37] M. Kawamura, H. Takahashi, K. Sugihara, S. Masubuchi, K. Hamaya, and T. Machida, Electrical polarization of nuclear spins in a breakdown regime of quantum Hall effect, Appl. Phys. Lett. **90**, 022102 (2007).

[38] G. Yusa, K. Muraki, K. Takashina, K. Hashimoto, and Y. Hirayama, Controlled multiple quantum coherences of nuclear spins in a nanometre-scale device, Nature (London) **434**, 1001 (2005).

[39] O. Stern, N. Freytag, A. Fay, W. Dietsche, J. H. Smet, K. von Klitzing, D. Schuh, and W. Wegscheider, NMR study of the electron spin polarization in the fractional quantum Hall effect of a single quantum well: Spectroscopic evidence for domain formation, Phys. Rev. B **70**, 075318 (2004).

[40] W. Desrat, D. K. Maude, M. Potemski, J. C. Portal, Z. R. Wasilewski, and G. Hill, Resistively detected nuclear magnetic resonance in the quantum Hall regime: Possible evidence for a skyrme crystal, Phys. Rev. Lett. **88**, 256807 (2002).